

MOTIF-RF: Multi-template On-chip Transformer Synthesis Incorporating Frequency-domain Self-transfer Learning for RFIC Design Automation

Houbo He^{1*}, Yizhou Xu^{1*}, Lei Xia¹, Yaolong Hu¹, Fan Cai², Taiyun Chi¹

¹ECE Department, Rice University, Houston, TX, USA ²Keysight Technologies, Santa Rosa, CA, USA

*Equally Credited Authors (ECAs)

{hh68, yx103, lx27, yh72, taiyun.chi}@rice.edu, fan.cai@keysight.com

Abstract—This paper presents a systematic study on developing multi-template machine learning (ML) surrogate models and applying them to the inverse design of transformers (XFMRs) in radio-frequency integrated circuits (RFICs). Our study starts with benchmarking four widely used ML architectures, including MLP-, CNN-, UNet-, and GT-based models, using the same datasets across different XFMR topologies. To improve modeling accuracy beyond these baselines, we then propose a new frequency-domain self-transfer learning technique that exploits correlations between adjacent frequency bands, leading to $\sim 30\%$ – 50% accuracy improvement in the S-parameters prediction. Building on these models, we further develop an inverse design framework based on the covariance matrix adaptation evolutionary strategy (CMA-ES) algorithm. This framework is validated using multiple impedance-matching tasks, all demonstrating fast convergence and trustworthy performance. These results advance the goal of AI-assisted “specs-to-GDS” automation for RFICs and provide RFIC designers with actionable tools for integrating AI into their workflows.

Index Terms—AI, CNN, design automation, graph transformer, inverse design, surrogate model, transfer learning, UNet, XFMR.

I. INTRODUCTION

The rapid evolution of AI has sparked growing interest in AI-assisted design automation within the RFIC design community [1]–[9]. This emerging paradigm promises to significantly enhance design productivity compared with the conventional manual design flow and lower barriers to entry for fresh graduates and less-experienced designers.

A critical distinction between RFIC and low-frequency analog IC design lies in the *extensive use of passive networks* [10]. These passive networks perform key circuit functions at RF, such as impedance matching, filtering, power combining or dividing, harmonic shaping, and more. Automating the design of passive networks is therefore a critical step towards realizing a fully automated RFIC design flow.

As shown in Fig. 1, the process of AI-assisted passive network design automation typically involves two stages. First, ML surrogate models are trained to replace time-consuming EM solvers used in the conventional design flow, enabling rapid yet accurate performance evaluation. Second, inverse design algorithms are applied, generating layouts that meet

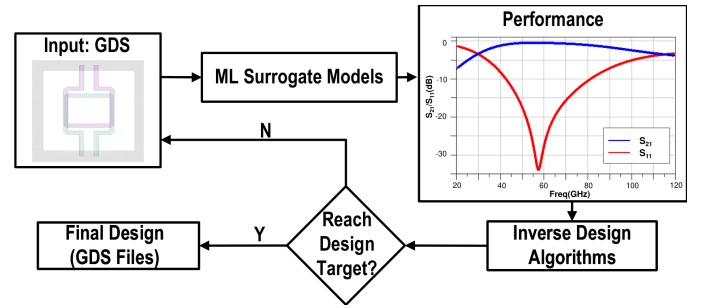


Fig. 1. “Specs to GDS” for AI-assisted design automation of XFMRs in RFICs, incorporating forward surrogate models and inverse design algorithms.

target specifications. This automated design process is also referred to as “specs to GDS” [1].

For RFICs, on-chip transformers (XFMRs), i.e., magnetically coupled coils, are the most widely used components for passive network synthesis [11]–[13]. While several recent studies have demonstrated the feasibility of building ML surrogate models to enable inverse design of XFMRs [6]–[8], they still face three major limitations: (1) Advanced ML architectures, such as Graph Transformers (GT), and the modeling of spectral continuity, remain largely underexplored in this context. (2) A comprehensive comparison of different ML models evaluated on *the same XFMR dataset* is missing. As a result, it is difficult for RFIC designers to evaluate the trade-offs among different models and select the most suitable one for their design needs. (3) The prediction accuracy of existing models is still limited. This results in noticeable discrepancies between ML-predicted and EM-simulated circuit performance especially at high frequency, limiting the practical *reliability* of applying such models for inverse design tasks.

This paper aims to address these gaps, and our three key contributions are summarized as follows.

- We offer a comprehensive, “handbook-style” evaluation of different ML surrogate models for XFMRs using the same dataset. Our goal is to provide RFIC designers, *regardless of their level of AI expertise*, with a clear understanding of these models, and enable informed decisions when integrating AI into their workflows.

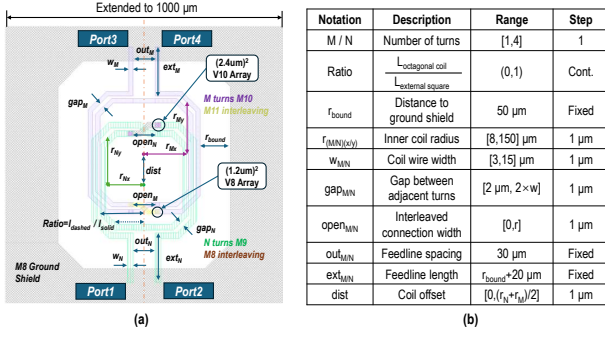


Fig. 2. (a) EM model of a generic $M:N$ XFMR and (b) its geometric parameters.

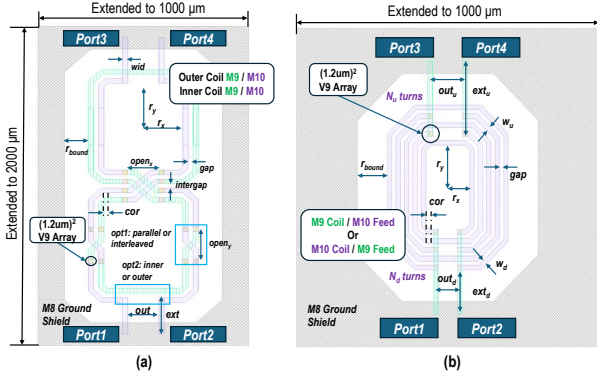


Fig. 3. (a) EM model of a generic 8-shaped-inductor-based XFMR. (b) EM model of a generic parallel-inductor-based XFMR.

- We propose a new frequency-domain self-transfer learning technique that leverages spectral continuity when training surrogate models, achieving a significant improvement in model prediction accuracy of $\sim 30\%$ – 50% .
- Using these surrogate models, we further demonstrate reliable inverse design through multiple impedance matching examples, where both the ML-predicted results and the EM-simulated results of the generated layouts closely align with the target specifications.

The remainder of this paper is organized as follows. Section II presents the background of XFMRs in RFIC design and outlines our data collection process. Section III introduces four ML surrogate models investigated in this study, including MLP, CNN, UNet, and GT, along with the proposed self-transfer learning technique. Section IV presents a comprehensive model evaluation and comparison. Section V demonstrates the inverse design flow using multiple impedance-matching examples. Section VI concludes this paper.

II. PRELIMINARIES

A. XFMR Fundamentals and S -parameters

A typical XFMR consists of two windings – a primary winding and a secondary winding that are magnetically coupled. The EM model of a generic $M:N$ XFMR is shown in Fig. 2(a), with its geometric design parameters summarized in Fig. 2(b). Other than the generic $M:N$ XFMRs, other XFMR topologies

have also been adopted by the RFIC industry. For example, the 8-shaped-inductor-based XFMR in Fig. 3(a) offers significantly enhanced EMI immunity due to its rejection of adjacent magnetic fields [13], and the parallel-inductor-based XFMR in Fig. 3(b) offers a stronger magnetic coupling with a higher passive efficiency at lower frequencies [14].

In the conventional manual design flow [15], XFMRs are analyzed using EM simulation software packages such as Cadence EMX, Keysight Momentum, or Ansys HFSS. These tools generate S -parameters, which are then imported into circuit simulators to evaluate circuit-level performance, such as inductance (L), quality factor (Q), impedance (Z), and loss over frequency [16]. As EM simulation is computationally intensive, it has become a major productivity bottleneck in RFIC design. Although prior work has explored ML surrogate models to predict L and Q [6]–[8], the capability to directly predict broadband S -parameters remains underdeveloped. As S -parameters are the most fundamental representation of XFMRs, from which nearly all performance characteristics can be derived [17], our work focuses on building surrogate models to directly predict S -parameters. Such capability is a critical prerequisite towards enabling efficient and reliable inverse design of the whole RFIC.

B. Dataset Generation

We prepared four datasets in this study: 5k samples for 1:1 XFMRs; 16k samples for generic $M:N$ XFMRs, with 1k samples for each configuration where M and N range up to 4; 5k samples for parallel-inductor-based XFMRs; and 5k samples for 8-shaped-inductor-based XFMRs. The EM-simulated four-port S -parameters, spanning from 0.5/1 to 100/200 GHz with a 0.5/1-GHz step, are used as labels of the datasets (only the 1:1 XFMR dataset includes data up to 200 GHz). This data collection process was done using Cadence EMX, taking about 80 hours in total with 16 threads. Due to the layout symmetry and reciprocity of passive networks [17], only six out of the 16 S -parameters (i.e., S_{11} , S_{12} , S_{13} , S_{14} , S_{33} , S_{34}) are required to fully represent the four-port network. Each S -parameter is separated into real and imaginary components, resulting in a total dimensionality of $6 \times 2 \times 200 = 2,400$.

It is important to note that all our datasets are generated based on the GlobalFoundries 22FDX process, a 22-nm CMOS SOI process that occupies significant market shares in automotive radar, IoT, 5G cellular communication, and other RF applications. This provides a realistic and industry-relevant basis for our study. This workflow could also be migrated to other technology nodes.

III. SURROGATE MODELING

This section first outlines our ML surrogate models based on four different NN architectures: MLP, CNN, UNet, and GT. We then present the proposed frequency-domain self-transfer learning technique to enhance the model accuracy.

A. ML Surrogate Models

1) *Tabular-based Method Using Multi-layer Perceptron (MLP)*: Our first modeling approach leverages an MLP neural

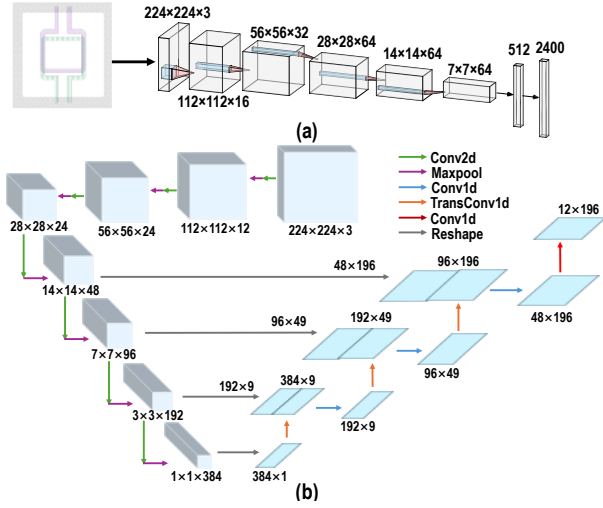


Fig. 4. (a) CNN-based and (b) UNet-based model architectures.

network, where the input features are tabular-based geometric parameters [as listed in Fig. 2(b)], and the outputs are the predicted real and imaginary components of the S-parameters. This method is straightforward and efficient, and serves as a baseline for evaluating more complex models.

2) *Image-based Methods Using CNN and UNet*: The second approach treats XFMR layouts as images, enabling the application of image-based deep learning techniques such as CNN [3] and U-Net [4]. These models leverage the spatial structure inherent in the layouts to learn intricate geometric features that govern the EM behavior of XFMRs. As such, they are more advantageous in modeling complex multi-turn topologies and spatial dependencies that may be difficult to capture through tabular representations alone. The architectures of these models are shown in Fig. 4.

3) *Graph Transformer (GT)-based Method*: The third approach leverages the recently developed GT architecture, which excels in capturing topological properties of graph-structured data, making them particularly well-suited for circuit modeling. We adopted an approach similar to [18], which employs Laplacian Summation Positional Encoding (LSPE) to capture graph topological features. In our implementation, each metal segment of the XFMR is represented as a token, characterized by six geometric parameters and an LSPE encoding. These tokens form the input of the GT model, as shown in Fig. 5(a). Connections between adjacent nodes are represented by weighted edges, with edge weights determined by the lengths of the corresponding metal traces. This encoding scheme allows the model to distinguish between different XFMR sizes and shapes based on positional features. As shown in Fig. 5(b), The tokens are vectorized, upsampled, and passed to the transformer encoder. This encoder follows the transformer framework [19], where each layer comprises a multi-head attention mechanism and a feedforward neural network. The encoded tokens for all XFMR segments are then concatenated to form a unified representation of the XFMR,

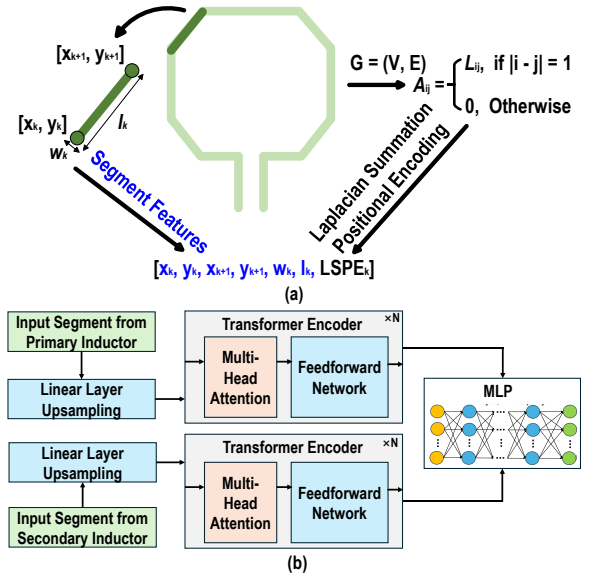


Fig. 5. (a) XFMR segment embedding. (b) GT-based model architecture.

followed by an MLP to map the extracted features to the corresponding S-parameters.

B. Proposed Frequency-domain Self-transfer Learning

Conventional ML surrogate models for predicting S-parameters typically treat each frequency point independently, which ignores the *spectral continuity governed by the underlying physics*. Although prior work such as STCNN [20] attempts to address this by adding a spectral convolutional layer, this layer is embedded as a hidden layer that lacks interpretability and no guarantee of capturing true frequency-domain correlations [21] [22].

In this work, we propose an iterative self-transfer learning technique, which explicitly leverages the correlation between adjacent frequency bands to improve model accuracy. Unlike conventional transfer learning or self-supervised learning methods [23], *our approach transfers knowledge learned from neighboring frequency bands within the same model*, allowing it to capture the spectral continuity more effectively. The detailed process is shown in Algorithm 1.

IV. MODEL EVALUATION

This section presents a comprehensive evaluation of all models introduced in Section III. All models were trained using the same loss function [20], defined as

$$L_{freq} = \frac{1}{N} \sum_{n=1}^N \sqrt{\frac{1}{K} \sum_{k=1}^K (S_{n,k} - \hat{S}_{n,k})^2} \quad (1)$$

where $k = 1, \dots, 200$ represents the frequency dimension, and $n = 1, \dots, 12$ represents the dimension of S-parameters.

A critical metric for comparing different models is accuracy measured by mean absolute error (MAE). To benchmark accuracy, we calculated the average MAE across all 12 S-parameter components at a single frequency point, denoted as

Algorithm 1: Iterative Self-transfer Learning Across Frequency Sub-bands

Data: Number of sub-bands N_{band} , maximum frequency f_{max} , number of transfer iterations T
Divide the full frequency range into N_{band} sub-bands;
Define each sub-model $[i]$ to cover frequency range $\left(\frac{(i-1) \cdot f_{\text{max}}}{N_{\text{band}}}, \frac{i \cdot f_{\text{max}}}{N_{\text{band}}}\right]$;
Train sub-model $[1]$ using data from the first sub-band;
Initialize transfer iteration counter $t = 1$;
while $t \leq T$ **do**
 Forward Transfer Training::
 for $i = 1$ **to** $N_{\text{band}} - 1$ **do**
 Initialize sub-model $[i+1]$ with sub-model $[i]$;
 Train sub-model $[i+1]$ on sub-band $i+1$ data;
 Backward Transfer Training::
 for $i = N_{\text{band}} - 1$ **down to** 1 **do**
 Initialize sub-model $[i]$ with sub-model $[i+1]$;
 Train sub-model $[i]$ on sub-band i data;
 Increment transfer iteration counter $t \leftarrow t + 1$;
return Final trained sub-models sub-model $[1 \dots N_{\text{band}}]$;

TABLE I
EVALUATION ON THE 1:1 XFMR DATASET

Trained Model	MLP	CNN	UNet	GT
Params	2.02M	2.93M	2.03M	1.95M
R^2	0.978	0.972	0.978	0.987
$\text{MAE}_{\text{avg},200\text{G}}$	0.0214	0.0252	0.0222	0.0164
$\text{MAE}_{\text{avg},2\text{SRF}}$	0.0135	0.0151	0.0144	0.0103

MAE_{freq} . Additionally, we report two forms of MAE_{avg} averaged over a frequency range: $\text{MAE}_{\text{avg},100\text{G}}$ (or $\text{MAE}_{\text{avg},200\text{G}}$ for 1:1 XFMRs) and $\text{MAE}_{\text{avg},2\text{SRF}}$. The former is calculated over the full range of 100 (or 200) GHz, while the latter is calculated only up to $2 \times$ the self-resonant frequency (SRF) of each XFMR. As XFMRs are typically used below their SRF in practice [24], $\text{MAE}_{\text{avg},2\text{SRF}}$ is a more relevant measure of modeling accuracy for real-world applications. The extended frequency range from SRF to $2 \times \text{SRF}$ captures harmonic behaviors that can be useful for nonlinear circuits.

A. Evaluation of Different Modeling Approaches

We started with the comparison for 1:1 XFMRs, with results summarized in Table I. These results lead to the following two key observations. (1) MLP- and GT-based models, which utilize geometric input features, outperform their image-based counterparts. This can be attributed to the relatively simple layout structure and low spatial complexity of 1:1 XFMRs. (2) Among models with similar model parameter counts ($\sim 2\text{M}$), GT-based model achieves the lowest $\text{MAE}_{\text{avg},2\text{SRF}}$ of 0.0103. This is likely attributed to GT's capability to extract latent structural features beyond basic coordinate inputs through graph positional encoding and attention mechanisms.

A similar comparison was made for generic $M:N$ XFMRs, with results summarized in Table II. Compared to 1:1 XFMRs, the increased design space and spatial complexity of $M:N$

TABLE II
EVALUATION ON THE GENERIC $M:N$ XFMR DATASET

Trained Model	MLP	CNN	UNet	UNet	GT
Params	2.02M	2.93M	2.03M	3.61M	3.53M
R^2	0.886	0.835	0.887	0.911	0.890
$\text{MAE}_{\text{avg},100\text{G}}$	0.0638	0.0803	0.0619	0.0513	0.0614
$\text{MAE}_{\text{avg},2\text{SRF}}$	0.0244	0.0333	0.0252	0.0180	0.0252

TABLE III
EVALUATION ON THE PARALLEL-INDUCTOR-BASED XFMR DATASET

Trained Model	MLP	CNN	UNet	GT
Params	2.02M	2.93M	2.03M	2.52M
R^2	0.995	0.985	0.982	0.871
$\text{MAE}_{\text{avg},100\text{G}}$	0.0099	0.0182	0.0197	0.0583
$\text{MAE}_{\text{avg},2\text{SRF}}$	0.0080	0.0149	0.0180	0.0521

XFMRs allow image-based methods, especially the UNet-based model, to catch up with and even outperform the baseline MLP-based model, particularly when the parameter counts are increased to reach saturated MAE. This demonstrates the advantage of image-based methods in modeling complex layouts with larger degrees of freedom.

Results for parallel-inductor-based and 8-shape-inductor-based XFMRs are presented in Table III and Table IV, respectively. For these two pre-defined templates, MLP-based approach achieves the lowest MAE_{avg} . The relatively complicated contours of XFMR metal segments makes the GT-based modeling less effective.

Additionally, we observe a limitation regarding the implemented linear transformer architecture. While GT-based model performs well when operating on relatively small geometrically encoded inputs, it struggles with more complex graphs, especially when extended to include additional layout encodings beyond single-layer metal traces such as *multi-layer routings and vias*. This observation is consistent with prior literature [25] [26], which note that transformer models demand large datasets and carefully engineered structural encodings [27] [28] to scale well beyond simple or medium-sized graph scenarios.

B. Evaluation of Frequency-domain Self-transfer Learning

To evaluate the accuracy improvement enabled by our proposed self-transfer learning technique, we conducted an experiment on the generic $M:N$ XFMR dataset. Fig. 6(a) plots how MAE_{freq} evolves over 10 iterations, and Fig. 6(b) summarizes the corresponding $\text{MAE}_{\text{avg},100\text{G}}$ when the number of frequency sub-bands (N_{band}) was set to 10. These results clearly demonstrate the effectiveness of iterative self-transfer learning in improving model accuracy.

Fig. 7 further explores the impact of varying N_{band} . When N_{band} is small, each sub-model is separated by a large frequency difference, thus limiting the effectiveness of inter-band knowledge transfer. On the other hand, when N_{band} becomes too large, each sub-model spans a narrow frequency range, reducing the frequency diversity needed to train each sub-model reliably. These results suggest that there exists an optimal N_{band} , which is 10 in this experiment. At this setting,

TABLE IV
EVALUATION ON THE 8-SHAPED-INDUCTOR-BASED XFMR DATASET

Trained Model	MLP	CNN	UNet	GT
Params	2.02M	2.93M	2.03M	2.49M
R^2	0.992	0.986	0.976	0.925
$MAE_{avg,100G}$	0.0108	0.0147	0.0191	0.0312
$MAE_{avg,2SRF}$	0.0060	0.0081	0.0119	0.0217

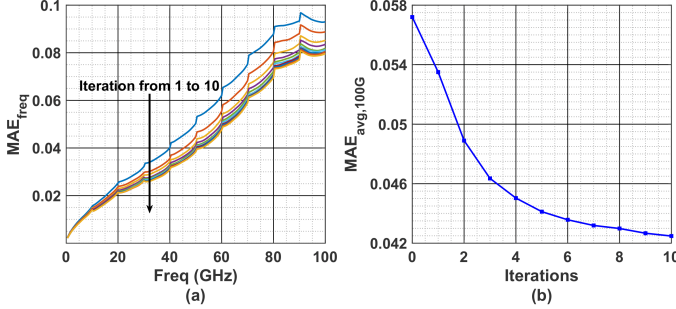


Fig. 6. (a) MAE_{freq} in each iteration, and (b) $MAE_{avg,100G}$ vs. iterations.

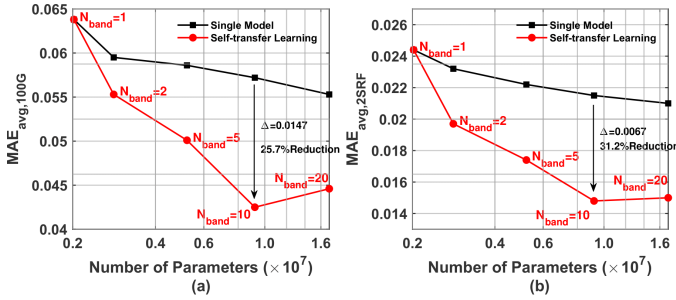


Fig. 7. Evaluation of self-transfer learning against N_{band} .

$MAE_{avg,2SRF}$ drops from 0.0215 to 0.0148, a 31% reduction in error compared to the baseline MLP-based model with the same number of model parameters.

Table V presents a comparison of model accuracy with and without the proposed frequency-domain self-transfer learning across all datasets, using the best-performing baseline model for each dataset. With the self-transfer learning technique, a consistent model accuracy improvement of more than 30% in $MAE_{avg,2SRF}$ is achieved. These improved models are then applied to the inverse design tasks presented in the following Section.

V. INVERSE DESIGN

We illustrate the inverse design of XFMRs by assigning an impedance-matching task as design target, as impedance matching is a foundational requirement in almost all RFIC designs [29], [30]. The following sub-sections present our cost function, model accuracy requirement, and several exemplar demonstrations.

A. Impedance-matching Task and Its Cost Function

In this work, we focus on the differential-mode operation of XFMRs, as RFICs usually employ differential circuits [31] to enable robustness against common-mode noise (e.g., noise on supply and ground lines). The design objective is to determine the optimal XFMR layout based on the target

TABLE V
MODEL ACCURACY COMPARISON WITH AND WITHOUT THE PROPOSED FREQUENCY-DOMAIN SELF-TRANSFER LEARNING

Dataset	1 : 1	M : N	Parallel	8-Shaped
Trained Model	GT	UNet	MLP	MLP
$MAE_{avg,2SRF}$, w/o	0.0099	0.0149	0.0061	0.0043
$MAE_{avg,2SRF}$, w/	0.0065	0.0103	0.0029	0.0021
Error Reduction	34.3%	30.9%	52.4%	51.2%

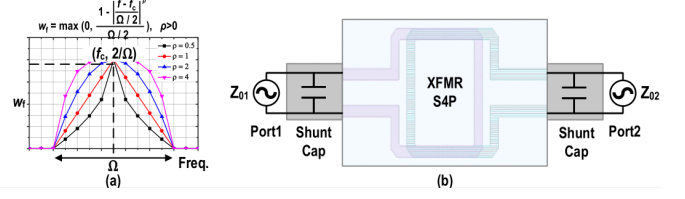


Fig. 8. (a) Window function w_f . (b) Adding shunt capacitors for matching.

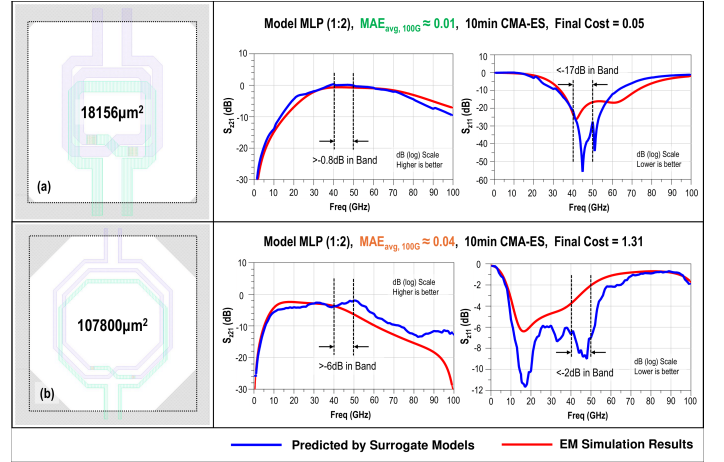


Fig. 9. Comparison of inverse design quality for a typical impedance-matching task using the 1:2 XFMR topology with different levels of accuracy. Design target: $f_c = 45$ GHz, $\Omega = 10$ GHz, $\rho = 1$, $Z_{01} = (40 - 50j)$ Ω , $Z_{02} = (150 + 80j)$ Ω .

source impedance Z_{01} , load impedance Z_{02} , center frequency f_c , and bandwidth Ω . To evaluate inverse design quality, we define a custom cost function, as

$$J_S = w_0 A + \sum_{f \in \Omega} w_f \left(w_1 |\Gamma_{in}| + w_2 \left(1 - |L| \right) \right) \quad (2)$$

Here, w_0 , w_1 , w_2 are weights assigned to the layout area (A), input reflection coefficient (Γ_{in}), and loss (L), respectively. Γ_{in} and L can be readily derived from the S-parameters [32]. In practice, a well-designed impedance-matching circuit should present $|\Gamma_{in}| < -10$ dB, and L should be as close to 0 dB as possible [17]. w_f is a frequency-domain window function, defined and illustrated in Fig. 8(a). By adjusting the window index ρ , the bandwidth profile of the cost function can be shaped to accommodate different bandwidth specifications. Additionally, we incorporate shunt capacitors into the XFMR-based matching network [Fig. 8(b)] to compensate reactive components and achieve broadband impedance transformation, a common practice in RFIC designs [33].

B. Inverse Design Reliability vs. Surrogate Model Accuracy

To evaluate the reliability of inverse design using ML surrogate models, we first conducted experiments with models of

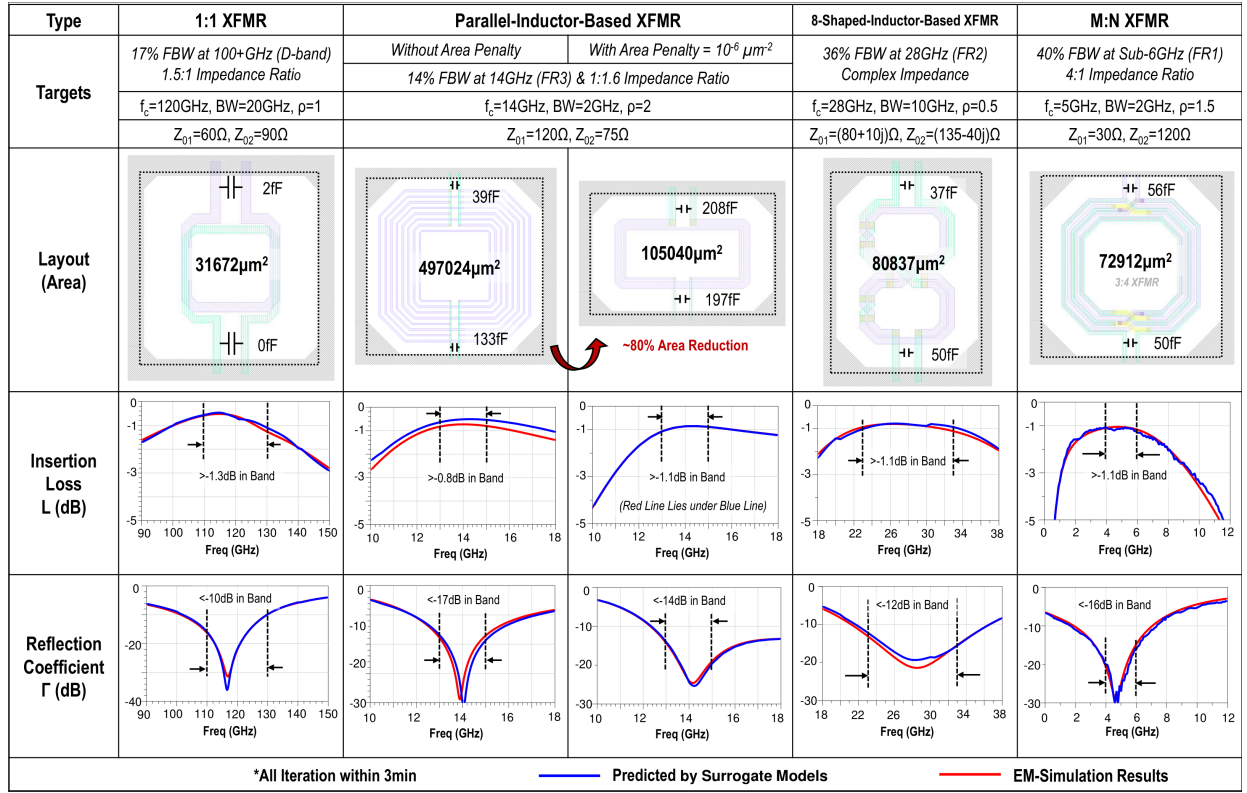


Fig. 10. Four inverse design examples using XFMRs for impedance matching, each with a different XFMR topology and a different application scenario.

different levels of accuracy. Fig. 9 shows a representative example using the 1:2 XFMR topology. Using a highly accurate surrogate model with an $\text{MAE}_{\text{avg},100\text{G}}$ of about 0.01 [Fig. 9(a)], the optimization target is successfully achieved. On the other hand, with a less accurate model with a high $\text{MAE}_{\text{avg},100\text{G}}$ of about 0.04 [Fig. 9(b)], the optimization task fails, and there exists an obvious discrepancy between EM-simulated and ML-model-predicted performance. Based on this result and similar experiments we conducted, an $\text{MAE}_{\text{freq}} < 0.01$ at the targeted frequency is generally required to produce meaningful and trustworthy inverse designs. This also justifies our proposed self-transfer learning technique, which greatly improves the model accuracy to meet this threshold.

C. Inverse Design Examples with Different XFMR Topologies

In this sub-section, we present four inverse design examples (Fig. 10), each showcasing a different XFMR topology and targeting different application scenarios with different specifications in terms of center frequency, bandwidth, and impedance transformation ratio. The selected center frequencies of these examples cover a variety of use cases, spanning 5G communication bands (in FR1 and FR2) and beyond-5G communication bands (in FR3 and D-band).

We adopt the Covariance Matrix Adaptation Evolution Strategy (CMA-ES) algorithm [34] in this work, which dynamically adjusts both the covariance matrix and step size during optimization. In repeated experiments, using 4 CPU

cores, our framework consistently converged to near-optimal cost values within three minutes.

VI. CONCLUSION

This paper presents a comprehensive evaluation of ML surrogate modeling and its application to the inverse design of XFMRs in RFICs. Specifically, we investigated four ML surrogate models, including MLP, CNN, UNet, and GT, on the same dataset and across multiple XFMR topologies. Additionally, we developed a frequency-domain self-transfer learning technique that significantly enhances model accuracy.

Our experiments showed that achieving an MAE_{freq} below 0.01 is essential to enable trustworthy inverse design. We also validated our end-to-end inverse design process using multiple impedance-matching tasks and further explored the area-performance trade-off. With CMA-ES optimization, all the experimental results demonstrated fast convergence and high-quality inverse designs from specs to GDS.

The surrogate modeling and inverse design approaches presented in this paper not only highlight the potential of AI-assisted design automation for RFICs but also offer a practical guide for RFIC designers who are seeking to integrate ML into their workflows.

REFERENCES

- [1] H. Chae, S. Chai, T. Chi, S. Li, and D. Pan, "ML-Assisted RF IC Design Enablement: the New Frontier of AI for EDA," in *Proc. Asia and South Pacific Design Automation Conf. (ASP-DAC)*, Jan. 2025, pp. 683–689.
- [2] E. A. Karahan *et al.*, "Deep-Learning Enabled Generalized Inverse Design of Multi-Port Radio-Frequency and Sub-Terahertz Passives and Integrated Circuits," *Nature Communications*, vol. 15, no. 1, Dec 2024.
- [3] E. A. Karahan, Z. Liu, and K. Sengupta, "Deep-Learning-Based Inverse-Designed Millimeter-Wave Passives and Power Amplifiers," *IEEE J. Solid-State Circuits*, vol. 58, no. 11, pp. 3074–3088, 2023.
- [4] H. Chae, H. Yu, S. Li, and D. Z. Pan, "PulseRF: Physics-Augmented ML Modeling and Synthesis for High-Frequency RFIC Design," in *Proc. IEEE/ACM Int. Conf. on Computer-Aided Design (ICCAD)*, Oct. 2024, pp. 1–9.
- [5] S. Chai, H. Chae, H. Yu, D. Z. Pan, and S. Li, "A D-Band InP Power Amplifier Featuring Fully AI-Generated Passive Networks," *IEEE Microw. Wireless Compon. Lett.*, vol. 35, no. 6, pp. 824–827, 2025.
- [6] D. Munzer, S. Er, M. Chen, Y. Li, N. S. Mannem, T. Zhao, and H. Wang, "Residual Network Based Direct Synthesis of EM Structures: A Study on One-to-One Transformers," in *Proc. IEEE Radio Freq. Integr. Circuits Symp. (RFIC)*, 2020, pp. 143–146.
- [7] C. Chu, Y. Mao, and H. Wang, "Transfer Learning Assisted Fast Design Migration Over Technology Nodes: A Study on Transformer Matching Network," in *Proc. IEEE/MTT-S Int. Microw. Symp. (IMS)*, 2024, pp. 188–191.
- [8] F. Passos, N. Lourenço, E. Roca, R. Martins, R. Castro-López, N. Horta, and F. V. Fernández, "PACOSYT: A Passive Component Synthesis Tool Based on Machine Learning and Tailored Modeling Strategies Towards Optimal RF and mm-Wave Circuit Designs," *IEEE J. Microw.*, vol. 3, no. 2, pp. 599–613, 2023.
- [9] L. Mendes, J. Silva, N. Lourenço, J. C. Vaz, R. Martins, and F. Passos, "Fully Automatically Synthesized mm-Wave Low-Noise Amplifiers for 5G/6G Applications," *IEEE Trans. Microwave Theory Tech.*, vol. 73, no. 8, pp. 4828–4841, 2025.
- [10] T. Chi, Y. Hu, X. Zhang, and H. Guo, "Pushing the Performance Boundaries of MmWave and Sub-THz Transceiver Circuits Through Passive Network Design Innovations," in *Proc. IEEE Int. Midwest Symp. Circuits Syst. (MWSCAS)*, 2024, pp. 759–763.
- [11] J. Long, "Monolithic Transformers for Silicon RF IC Design," *IEEE J. Solid-State Circuits*, vol. 35, no. 9, pp. 1368–1382, 2000.
- [12] C. Li, M. Wang, T. Chi, A. Kumar, M. Boenke, D. Wang, N. Cahoon, A. Bandyopadhyay, A. Joseph, and H. Wang, "5G mm-Wave front-end-module design with advanced SOI process," in *Proc. IEEE Int. Conf. on ASIC (ASICON)*, 2017, pp. 1017–1020.
- [13] P. Guan, H. Jia, W. Deng, T. Siriburanon, R. B. Staszewski, Z. Wang, and B. Chi, "8-Shaped Inductors: An Essential Addition to RFIC Designers' Toolbox," *IEEE Open J. Solid-State Circuits Soc.*, vol. 4, pp. 131–146, 2024.
- [14] C. C. Lim, K. S. Yeo, K. W. Chew, S. F. Lim, C. C. Boon, Qiu-ping, M. A. Do, and L. Chan, "An Area Efficient High Turn Ratio Monolithic Transformer for Silicon RFIC," in *Proc. IEEE Radio Freq. Integr. Circuits Symp. (RFIC)*, 2008, pp. 167–170.
- [15] Y. Hu, H. Guo, S. Wang, J. Liu, W. Cao, and T. Chi, "AdreamDCO: AI-Driven Robust and Efficient Design Automation for Digitally Controlled Oscillators," in *Proc. 62nd ACM/ESDA/IEEE Design Autom. Conf. (DAC)*, Jun. 2025, pp. 1–7.
- [16] X. Zhang, S. Li, D. Huang, and T. Chi, "A Millimeter-Wave Three-Way Doherty Power Amplifier for 5G NR OFDM," *IEEE J. Solid-State Circuits*, vol. 58, no. 5, pp. 1256–1270, 2023.
- [17] D. M. Pozar, *Microwave Engineering*, 4th ed. Hoboken, NJ, USA: Wiley, 2011.
- [18] D. Kim, J. Park, Y. Oh, and B. Hwang, "Traceformer: S-parameter Prediction Framework for PCB Traces Based on Graph Transformer," *Proc. 61st ACM/ESDA/IEEE Design Autom. Conf. (DAC)*, p. 1–6, Jun. 2024.
- [19] A. Vaswani, N. Shazeer, N. Parmar, J. Uszkoreit, L. Jones, A. N. Gomez, L. u. Kaiser, and I. Polosukhin, "Attention is All you Need," in *Proc. Adv. Neural Inf. Process. Syst. (NeurIPS)*, vol. 30, 2017.
- [20] H. M. Torun, H. Yu, N. Dasari, V. C. K. Chekuri, A. Singh, J. Kim, S. K. Lim, S. Mukhopadhyay, and M. Swaminathan, "A Spectral Convolutional Net for Co-Optimization of Integrated Voltage Regulators and Embedded Inductors," in *Proc. IEEE/ACM Int. Conf. on Computer-Aided Design (ICCAD)*, Oct. 2019, pp. 1–8.
- [21] Y. Bengio, A. Courville, and P. Vincent, "Representation Learning: A Review and New Perspectives," *IEEE Trans. Pattern Anal. Mach. Intell.*, vol. 35, no. 8, pp. 1798–1828, 2013.
- [22] Z. C. Lipton, "The Mythos of Model Interpretability," *Commun. ACM*, vol. 61, no. 10, pp. 36–43, 2018.
- [23] Z. Zhao, L. Alzubaidi, J. Zhang, Y. Duan, and Y. Gu, "A comparison review of transfer learning and self-supervised learning: Definitions, applications, advantages and limitations," *Expert Syst. Appl.*, vol. 242, p. 122807, May 2024.
- [24] H. Guo, Y. Hu, and T. Chi, "34.4 A 9.05-to-37.0GHz LO Generator with Magnetic Mode Switching and Tuning-Free Octave-Bandwidth Common-Mode Resonator Achieving > 190.7dBc/Hz FoM," in *Proc. IEEE Int. Solid-State Circuits Conf. (ISSCC)*, vol. 68, 2025, pp. 560–562.
- [25] L. Rampášek, M. Galkin, V. P. Dwivedi, A. T. Luu, G. Wolf, and D. Beaini, "Recipe for a General, Powerful, Scalable Graph Transformer," in *Proc. Adv. Neural Inf. Process. Syst. (NeurIPS)*, vol. 35, 2022, pp. 16 659–16 673.
- [26] V. P. Dwivedi and X. Bresson, "A Generalization of Transformer Networks to Graphs," in *Proc. AAAI Workshop on Deep Learning on Graphs: Methods and Applications (DLG-AAAI)*, 2021.
- [27] C. Ying, T. Cai, S. Luo, S. Zheng, and G. E. Karniadakis, "Do Transformers Really Perform Bad for Graph Representation?" *Proc. NeurIPS Workshop on Graph Representation Learning*, 2021.
- [28] V. P. Dwivedi, A. C. Louis, X. Bresson, and T. Laurent, "Graph Neural Networks with Learnable Structural and Positional Representations," *Proc. Int. Conf. Learn. Represent. (ICLR)*, 2022.
- [29] Y. Hu and T. Chi, "A 27–46-GHz Low-Noise Amplifier With Dual-Resonant Input Matching and a Transformer-Based Broadband Output Network," *IEEE Microw. Wireless Compon. Lett.*, vol. 31, no. 6, pp. 725–728, 2021.
- [30] Y. Hu, X. Zhang, Q. Zhou, F. Cai, C. Cui, and T. Chi, "Automated mmWave Power Amplifier Design Flow and a 28-GHz Design Example in 45-nm CMOS SOI," in *Proc. IEEE/MTT-S Int. Microw. Symp. (IMS)*, 2024, pp. 842–845.
- [31] S. Li, T. Chi, J.-S. Park, H. T. Nguyen, and H. Wang, "A 28-GHz Flip-Chip Packaged Chireix Transmitter With On-Antenna Outphasing Active Load Modulation," *IEEE J. Solid-State Circuits*, vol. 54, no. 5, pp. 1243–1253, 2019.
- [32] M. B. Steer, *Microwave and RF Design: Networks*. Raleigh, NC, USA: NC State University, 2019, vol. 3.
- [33] X. Zhang, H. Guo, and T. Chi, "A Millimeter-Wave Four-Way Doherty Power Amplifier With Over-GHz Modulation Bandwidth," *IEEE J. Solid-State Circuits*, vol. 59, no. 12, pp. 3898–3914, 2024.
- [34] N. Hansen and A. Ostermeier, "Adapting Arbitrary Normal Mutation Distributions in Evolution Strategies: The Covariance Matrix Adaptation," in *Proc. IEEE Int. Conf. Evol. Comput. (ICEC)*, 1996, pp. 312–317.